Microscopic model for the stacking-fault potential and the exciton wave function in GaAs

Mikhail V. Durnev,[1] Mikhail M. Glazov,[1] Xiayu Linpeng,[2] Maria L. K. Viitaniemi,[2] Bethany Matthews,[3] Steven R. Spurgeon,[3] Peter V. Sushko,[4] Andreas D. Wieck,[5] Arne Ludwig,[5] and Kai-Mei C. Fu[2,6]

[1]*Ioffe Institute, 194021 St. Petersburg, Russia*

[2]*Department of Physics, University of Washington, Seattle, Washington 98195, USA*

[3]*Energy and Environment Directorate, Pacific Northwest National Laboratory, Richland, Washington 99352, USA*

[4]*Physical and Computational Sciences Directorate, Pacific Northwest National Laboratory, Richland, Washington 99352, USA*

[5]*Lehrstuhl für Angewandte Festkörperphysik, Ruhr-Universität Bochum, D-44870 Bochum, Germany*

[6]*Department of Electrical Engineering, University of Washington, Seattle, Washington 98195, USA*

(Received 1 November 2019; accepted 28 February 2020; published 20 March 2020)

Two-dimensional stacking fault defects embedded in a bulk crystal can provide a homogeneous trapping potential for carriers and excitons. Here we utilize state-of-the-art structural imaging coupled with density-functional and effective-mass theory to build a microscopic model of the stacking-fault exciton. The diamagnetic shift and exciton dipole moment at different magnetic fields are calculated and compared with the experimental photoluminescence of excitons bound to a single stacking fault in GaAs. The model is used to further provide insight into the properties of excitons bound to the double-well potential formed by stacking fault pairs. This microscopic exciton model can be used as an input into models which include exciton-exciton interactions to determine the excitonic phases accessible in this system.

DOI: 10.1103/PhysRevB.101.125420

I. INTRODUCTION

The stacking fault (SF), a misordering of lattice planes in a crystal lattice, is a prevalent two-dimensional (2D) crystal defect which can affect the mechanical, optical, and electrical properties of a material [1–4]. While typically the macroscopic properties of a material are studied as a function of defect density [5], the recent isolation of large-scale ($\sim$10 μm) SFs in GaAs enabled the study of excitons bound to a single SF [6]. The high homogeneity of the excitonic emission, combined with the measured giant static dipole moment, indicate the atomically thin SF potential may be a promising platform for the realization of novel excitonic phases [7,8]. Due to the built-in static dipole moment, the excitons bound to the SFs in GaAs demonstrate the magneto-Stark effect: In the reference frame of an exciton moving across the magnetic field, an effective electric field appears which results in the Stark shift of the exciton energy. The magneto-Stark effect results in a nonreciprocal variation of the exciton energy in a magnetic field: For positive and negative directions of the magnetic field and fixed direction of exciton propagation, the energy shift has opposite signs [6]. As shown in earlier studies of excitons in bulk materials, this effect provides direct proof of exciton motion in the crystal [9,10]. It is also of importance in nonlinear optics in semiconductors, providing a mechanism of, e.g., second-harmonic generation on otherwise forbidden excitonic states [11].

To gain further insight into the magneto-optics of excitons, their lifetime and exciton-exciton interactions, knowledge of the confinement potential and wave function of the SF exciton is required. Advancements in structural imaging and density-functional theory (DFT) calculations, combined with our ability to optically isolate and characterize excitons on a single fault, provide an unprecedented opportunity to quantitiatively understand the SF exciton. As a result, in this paper we develop a microscopic model of the SF potential and SF exciton wave function in GaAs. Within this model, the exciton hole is localized at the SF plane and the electron is bound via Coulombic attraction to the hole. An electric field due to the spontaneous polarization across a single SF plane is modeled by a step function which results in the large electron-hole separation of about 10 nm. Variational method calculations based on this potential are found to be in reasonable agreement with experiment with respect to the observed diamagnetic shift and static dipole moment in single SFs. The model further provides an explanation for the twofold larger dipole moment observed in double-well potentials formed by SF pairs, suggesting that these double-well structures could provide further tunability in the excitonic properties.

The paper is organized as follows. In Sec. II, we present the structural images of the SFs via electron microscopy. Further, we present the microscopic model of the SF potential in Sec. III. Section IV provides a detailed comparison between the calculated excitonic properties of SFs with the experiment in terms of key parameters such as diamagnetic shifts and magneto-Stark effect, demonstrating the validity of the model. The paper is summarized with a brief conclusion in Sec. V.

II. STRUCTURAL IMAGING OF SINGLE AND DOUBLE STACKING FAULTS

Cross-sectional scanning transmission electron microscopy (STEM) analysis of two different SF defects, the pyramid and trapezoid, was performed to determine the structure of the defects. The experimental image is compared to the result of multislice image simulations based on *ab initio*

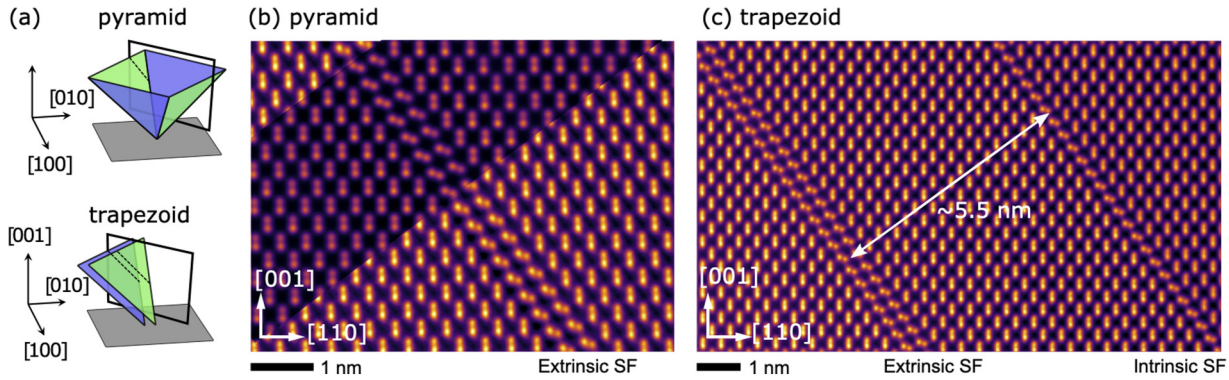

FIG. 1. (a) The geometry of the cross section of the STEM images. The black rectangles show the cross section plane and the dashed lines show where the stacking faults are. (b), (c) Cross-sectional STEM images of stacking faults in the pyramid and trapezoid samples. (b) is overlaid with multislice image simulations based on *ab initio* models, showing an excellent match between experiment and theory. These images are the result of nonrigid alignment and template matching, as described in Appendix A.

calculations (Appendix A); these results show an excellent agreement. The SFs are embedded in the GaAs epitaxial layer which is grown on a (100)-terminated GaAs substrate. The location of the faults are identified by oval defects at the surface [12]. The geometry of the cross-section with respect to the structure is shown in the insets of Fig. 1(a). As shown in Fig. 1(b), in the pyramid structure we observe an isolated SF plane parallel to the (111) plane. Based on these observations, it is confirmed that excitons are bound to a single, highly homogeneous SF in the pyramid structure. In contrast, the trapezoid structure shown in Fig. 1(c) exhibits closely spaced intrinsic-extrinsic SF pairs. In this particular trapezoid, the planes are separated by ∼5.5 nm in the [111]-type direction, but this distance can vary from one structure to another. Thus, for trapezoid structures, excitons are bound to a pair potential in which the SF separation is expected to impact the bound-exciton properties.

III. MICROSCOPIC MODEL

A. Single stacking fault at zero magnetic field

We first consider excitons bound to a single SF at zero magnetic field. The SF is positioned at $z = 0$, with $z \parallel [111]$, and occupies the xy plane with $x \parallel [11\bar{2}]$, $y \parallel [\bar{1}10]$. We consider excitons described by the wave function $\Psi_X = \psi(\boldsymbol{r}_e, \boldsymbol{r}_h) u_c(\boldsymbol{r}_e) u_v(\boldsymbol{r}_h)$, where u_c and u_v are the Bloch functions of the conduction band (Γ_6 representation of the T_d point group) and the heavy-hole valence subband ($\Gamma_8, \pm 3/2$ representation of the T_d point group), respectively, and $\psi(\boldsymbol{r}_e, \boldsymbol{r}_h)$ is the two-particle envelope function. Note, that the admixture of the light-hole component to the hole state in the exciton is negligible [6].

To obtain the exciton spectrum in the absence of a magnetic field, we solve the Schrödinger equation,

$$\mathcal{H}\psi = \varepsilon\psi, \tag{1}$$

for the exciton envelope function $\psi(\boldsymbol{r}_e, \boldsymbol{r}_h)$ and energy ε with the following Hamiltonian:

$$\mathcal{H} = \frac{\boldsymbol{p}_e^2}{2m_e} + \frac{p_{hx}^2 + p_{hy}^2}{2m_{h,\parallel}} + \frac{p_{hz}^2}{2m_{h,\perp}} + E_g + V_{\mathrm{SF}}(z_e, z_h) - \frac{e^2}{\varkappa|\boldsymbol{r}_e - \boldsymbol{r}_h|}. \tag{2}$$

Here $\boldsymbol{p}_{e,h} = -i\hbar\nabla_{e,h}$ are the electron and hole momentum operators; m_e, $m_{h,\parallel}$, and $m_{h,\perp}$ are the components of the electron and hole effective-mass tensors; E_g is the energy gap of the bulk material; V_{SF} is the SF potential experienced by the electron and hole; e is the electron charge; and $\varkappa$ is the static dielectric constant of the background medium. The electron effective mass is isotropic, whereas the heavy-hole effective-mass tensor has different components for the motion in the SF plane ($m_{h,\parallel}$) and in the z direction ($m_{h,\perp}$) [13–15].

We suggest that the presence of a single SF modifies the electron and hole bands, yielding a potential in the following form:

$$V_{\mathrm{SF}}(z_e, z_h) = V_0\Theta(-z_e) - V_0\Theta(-z_h) - u_0\delta(z_h), \tag{3}$$

where $\Theta(z)$ and $\delta(z)$ are the Heaviside and Dirac delta functions, respectively. V_0 and u_0 are positive parameters. This potential is sketched in Fig. 2(a). The model potential binds the hole in the z direction due to the δ-function term, but

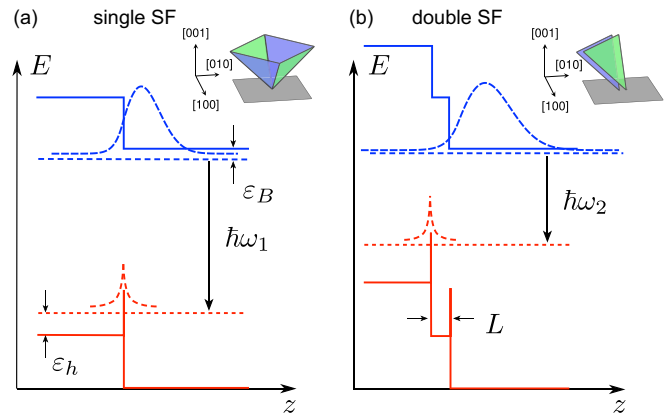

FIG. 2. Sketch of the conduction and valence band potentials for single (a) and double (b) stacking-fault structures (in the electron representation). The blue and red dashed lines schematically depict the z-distribution of electron and hole density in the exciton, respectively. ε_h denotes the hole binding energy and ε_B denotes the exciton binding energy. The insets illustrate the pyramid and trapezoid structures embedded in the crystal, z is in the direction perpendicular to the stacking fault plane.

does not bind the electron. The electron in the exciton is then attracted to the hole due to the Coulomb interaction. The parameter V_0 describes the band offset related to the presence of the built-in spontaneous electric polarization, and consequently the electric field, in the SF layer [16–18]. Thus, V_0 is equal to the electrostatic potential change across the SF. The delta-function term that confines the hole models the type-II band alignment, which is believed to appear between the GaAs zinc-blende and wurtzite phases [19–21]. The value of u_0 can be estimated as a product of the valence band offset between the zinc-blende and wurtzite phases of GaAs ΔE_v and the effective SF width $d_{\rm SF}$. Using $\Delta E_v = 117$ meV [20] and $d_{\rm SF} \sim 10$ Å, we obtain $u_0 \sim \Delta E_v d_{\rm SF} \sim 1$ eVÅ. The same delta-function term for the conduction band is neglected since it does not bind an electron and, hence, only slightly modifies electron wave function. We also note that there is an energetically close, second conduction band in the wurtzite phase of GaAs [20], however, this band is far in energy in a structure with a thin wurtzite layer surrounded by the zinc-blende crystal [22], and therefore is neglected in the following. The suggested potential agrees well with DFT calculations of the SF electrostatic potential and single-particle wave functions which predicts $V_0 \approx 10$ meV and a hole confinement length of ∼4 nm (see Appendix B for details).

The confinement energy of a hole bound to potential Eq. (3) is

$$\varepsilon_h = \varepsilon_0 \left(1 - \frac{V_0}{4\varepsilon_0}\right)^2, \tag{4}$$

where $\varepsilon_0 = m_{h,\perp} u_0^2/(2\hbar^2)$. The potential binds the hole if $V_0 < 4\varepsilon_0$, which is true for our system, where $V_0 \approx 10$ meV and $\varepsilon_h \approx 10$ meV (corresponding to $\varepsilon_0 \approx 15$ meV), as will be shown below. The localization length of the heavy hole in the z direction is $a_h \sim [2\hbar^2/(m_{h,\perp}\varepsilon_h)]^{1/2}$. To simplify the calculation, in the following we assume that $a_h = 0$, so the hole is tightly bound to the SF and $z_h = 0$. The validity of this assumption is supported by the ∼4 nm DFT hole confinement length, which is much less than the ∼20 nm exciton diameter. By contrast, the electron remains bound only due to the Coulomb interaction with the hole. Note that the model potential of ZnSe SFs suggested recently in Ref. [23] does not bind a hole. It may be related to large electric field inside the ZnSe SFs as compared to GaAs SFs (∼5 times larger), which prevents the binding of a hole [as described by Eq. (4) at $V_0 > 4\varepsilon_0$].

In the absence of an external magnetic field, the exciton envelope can be written as $\psi(\boldsymbol{r}_e, \boldsymbol{r}_h) = \varphi(\boldsymbol{r})\exp(i\boldsymbol{K}\boldsymbol{R})$, where $\boldsymbol{r} = \boldsymbol{r}_e - \boldsymbol{r}_h$ is the coordinate of relative motion (note that $z = z_e$), and $\boldsymbol{R}$ and $\boldsymbol{K}$ are the coordinate and the wave vector of the exciton center of mass in the SF plane. The effective Hamiltonian that acts on the exciton envelope function $\varphi(\boldsymbol{r})$ is

$$\mathcal{H}_0 = \frac{p_x^2 + p_y^2}{2\mu} + \frac{p_z^2}{2m_e} + V_0\Theta(-z) - \frac{e^2}{\varkappa|\boldsymbol{r}|}, \tag{5}$$

with $\mu^{-1} = m_e^{-1} + m_{h,\parallel}^{-1}$. The exciton center of mass dispersion is discussed further in Sec. III B.

To solve the Schrödinger equation with the Hamiltonian Eq. (5), we use the variational approach. We choose $\varphi(\boldsymbol{r})$ in the form

$$\varphi(\boldsymbol{r}) = \mathcal{N}\exp\left(-\sqrt{\frac{\rho^2}{a^2} + \frac{z^2}{c^2}}\right) f\left(\frac{z}{c}\right), \tag{6}$$

where $\boldsymbol{\rho} = (x, y)$, $\mathcal{N}$ is the normalization constant,

$$f(\xi) = (1 + \alpha\xi)\Theta(\xi) + e^{\alpha\xi}\Theta(-\xi), \tag{7}$$

and a, c, and α are variational parameters. The parameters a and c are the effective in-plane and z sizes of the exciton, the function $f(\xi)$ describes the asymmetric confinement of the electron. Correspondingly, the dimensionless parameter $\alpha > 0$ determines the asymmetry of the exciton wave function in the z direction, which is caused by the asymmetry of the electron distribution. The wave function Eq. (7) well describes the behavior of the electron z distribution with the change of V_0 in Eq. (3): At $\alpha = 0$, which corresponds to $V_0 = 0$, we have a symmetric distribution, $f(\xi) = 1$, and at $\alpha \gg 1$, which corresponds to large values of V_0, the wave function $f(\xi)$ vanishes at $\xi \leqslant 0$, and the electron does not penetrate the barrier.

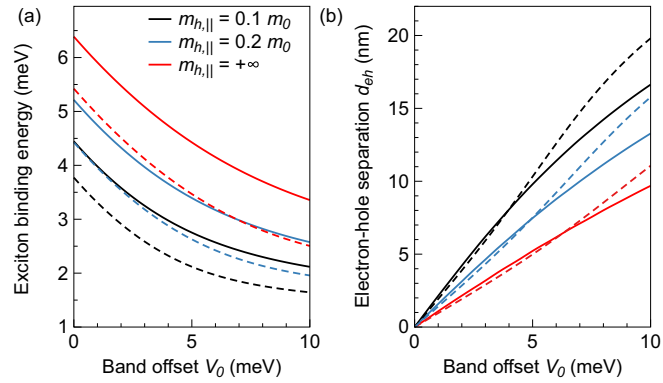

FIG. 3. Exciton binding energy (a) and electron-hole separation (b) as functions of the stacking fault band offset. Solid and dashed lines depict the results for the hydrogenlike and Gaussian trial exciton wave functions.

Figure 3 shows the results of our variational calculations for the Hamiltonian Eq. (5) and the trial function Eq. (6). We plot the exciton binding energy $\varepsilon_B = -\langle\varphi|\mathcal{H}_0|\varphi\rangle$ and the average distance between the electron and hole in the z direction $d_{eh} = \langle\varphi|z|\varphi\rangle$, as functions of the band offset V_0. In the calculations we use $m_e = 0.07\,m_0$, $\varkappa = 12$, and three different values for $m_{h,\parallel}$: $0.1\,m_0$, $0.2\,m_0$ and $+\infty$. The infinite case corresponds to an electron bound on a donor that is located at the SF plane.

Additionally, the dashed lines in Fig. 3(a) present the results using a simplified Gaussian-like trial wave function,

$$\tilde{\varphi}(\boldsymbol{r}) = \mathcal{N}\exp\left(-\frac{\rho^2}{2a^2} - \frac{z^2}{2c^2}\right) f\left(\frac{z}{c}\right), \tag{8}$$

with f given by Eq. (7). The binding energy of the Coulomb potential calculated using the Gaussian-like function is $E_B = (8/3\pi)$Ry, where $\mathrm{Ry} = m_e e^4/2\varkappa^2\hbar^2$, which is ≈15% smaller than the exact value. These two values are positioned on the red lines in Fig. 3(a) at $V_0 = 0$. By comparing solid and dashed lines in Fig. 3(a), we conclude that the trial wave function

Eq. (8) results in a 15–20% smaller exciton binding energy than the more accurate hydrogenlike wave function Eq. (6) also for $V_0 \neq 0$. However, the results for the electron-hole separation using the Gaussian-like trial function agree well with the ones obtained for the hydrogenlike trial function. This agreement motivates using a Gaussian-like trial wave function to calculate the electron-hole separation in the more complicated case where the magnetic field $\boldsymbol{B} \neq 0$.

B. Single stacking fault at nonzero magnetic field

An external magnetic field $\boldsymbol{B}$ applied in the SF plane brings the electron and hole closer and shrinks the exciton wave function. This results in the diamagnetic shift, which is quadratic in $\boldsymbol{B}$, and also in the decrease of d_{eh}, yielding the suppression of the magneto-Stark effect. In a wide range of magnetic fields applied in the experiment, these effects cannot be treated perturbatively. Thus, we now consider an exciton bound at the single SF in the presence of an external magnetic field $\boldsymbol{B} \parallel y$. The exciton Hamiltonian is obtained from Eq. (2) using the substitution $\boldsymbol{p}_e \to \boldsymbol{p}_e - (e/c)\boldsymbol{A}(\boldsymbol{r}_e)$ and $\boldsymbol{p}_h \to \boldsymbol{p}_h + (e/c)\boldsymbol{A}(\boldsymbol{r}_h)$, where $\boldsymbol{A}$ is the vector potential chosen to be the symmetric form $\boldsymbol{A}(\boldsymbol{r}) = B(z/2, 0, -x/2)$.

Since we assume the strong hole confinement in the z direction, we can neglect the influence of the in-plane magnetic field on the heavy-hole motion along the SF normal. Hence, the exciton diamagnetic shift including the field-induced variation of the average electron-hole separation is determined by the electron component. In the presence of a magnetic field $\boldsymbol{B} \parallel y$, the momentum of the exciton center of mass should be written as

$$P_x = -\mathrm{i}\hbar\frac{\partial}{\partial x_e} - \mathrm{i}\hbar\frac{\partial}{\partial x_h} - \frac{1}{2}m_e\omega_c z, \quad P_y = p_{ey} + p_{hy}, \tag{9}$$

where $\omega_c = |e|B/(m_e c)$ [24]; see also Refs. [25–27] in which quasi-2D excitons in an in-plane magnetic field were studied. The exciton envelope wave function then reads

$$\psi(\boldsymbol{r}, \boldsymbol{R}) = \exp\left[\mathrm{i}\left(P_x + \frac{1}{2}m_e\omega_c z\right)\frac{X}{\hbar} + \mathrm{i}P_y\frac{Y}{\hbar}\right]\varphi(\boldsymbol{r}). \tag{10}$$

Here P_x and P_y are the eigenvalues of the center of mass momentum operator in Eqs. (9).

Using the wave function Eq. (10) and the general Hamiltonian Eq. (2), we obtain the effective Hamiltonian that describes the internal motion of the exciton (at $P_x = P_y = 0$):

$$\mathcal{H}_B = \frac{[p_x + (m_e - \mu/2)\omega_c z]^2}{2m_e} + \frac{(p_z - \mu\omega_c x/2)^2}{2m_e} + \frac{(p_x - \mu\omega_c z/2)^2}{2m_{h,\parallel}} + \frac{p_y^2}{2\mu} + V_0\Theta(-z) - \frac{e^2}{\varkappa|\boldsymbol{r}|}. \tag{11}$$

To obtain the ground state of the exciton in a magnetic field, we use the following trial wave function:

$$\varphi_B(\boldsymbol{r}) = \mathcal{N}\exp\left(-\frac{x^2}{2a^2} - \frac{y^2}{2b^2} - \frac{z^2}{2c^2}\right)f\left(\frac{z}{c}\right), \tag{12}$$

with four variational parameters a, b, c, and α, and f given by Eq. (7). At $B = 0$, we have $a = b$ and this wave function coincides with Eq. (8). Although this wave function does not allow one to evaluate accurately the exciton binding energy at $B = 0$, it provides reasonable accuracy for the electron-hole separation and allows us to substantially simplify numerical calculations as discussed above. The diamagnetic shift of the exciton energy is then determined by

$$E_D = \langle\varphi_B|\mathcal{H}_B|\varphi_B\rangle - E_0, \tag{13}$$

where $E_0 = \langle\varphi_B|\mathcal{H}_B|\varphi_B\rangle$ at $B = 0$.

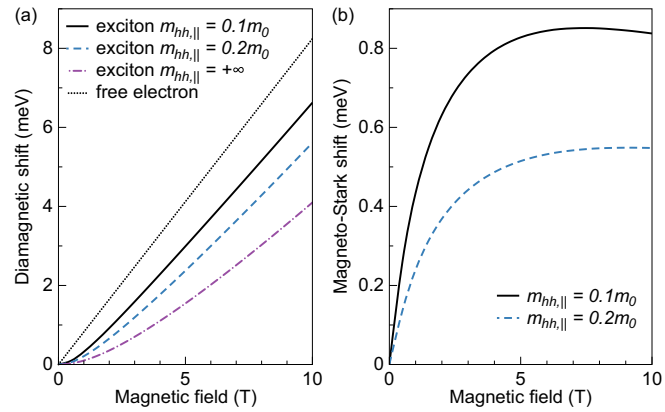

FIG. 4. Calculated exciton diamagnetic shift (a) and magneto-Stark shift (b) for different values of the hole in-plane mass $m_{hh,\parallel}$. The dotted line in panel (a) is the diamagnetic shift of a free electron ($\hbar\omega_c/2$). Here, $V_0 = 10$ meV.

To evaluate the magneto-Stark effect, we calculate the center of mass dispersion of the exciton making use of the following relations for the exciton velocity $\boldsymbol{v}(\boldsymbol{P})$ and the exciton kinetic energy $E(\boldsymbol{P})$ [24]:

$$\boldsymbol{v} = \frac{dE(\boldsymbol{P})}{d\boldsymbol{P}}, \quad \boldsymbol{P} = M\boldsymbol{v}(\boldsymbol{P}) - \frac{e}{c}[\boldsymbol{B}\times\boldsymbol{r}], \tag{14}$$

where $M = m_e + m_{h,\parallel}$ is the mass for exciton translational motion in the SF plane. Solving Eq. (14), we obtain

$$E(\boldsymbol{P}) = \frac{(P_x - eBd_{eh}/c)^2}{2M} + \frac{P_y^2}{2M}. \tag{15}$$

Here the electron-hole separation d_{eh} generally depends on the magnetic field. Equation (15) allows us to evaluate the magneto-Stark shift of the exciton energy as

$$E_S = -\frac{eP_xBd_{eh}}{Mc} = \beta' K_x B, \tag{16}$$

where the parameter $\beta' = -e\hbar d_{eh}/(Mc)$ describes the slope of the magneto-Stark shift and $K_x = P_x/\hbar$ is the x component of the exciton wave vector that is defined by the experiment geometry; see Eq. (19) in Sec. IV. At low magnetic fields, β' does not depend on the magnetic field and is determined by the electron-hole separation d_{eh} at $B = 0$, which is calculated in Sec. III A and shown in Fig. 3(b).

Figure 4 illustrates the dependence of the diamagnetic shift Eq. (13) and magneto-Stark shift Eq. (16) on the magnetic field. The magnetic field lying at the SF plane shrinks the exciton wave function in the xz plane and thus reduces the electron-hole separation d_{eh}. Therefore, the magneto-Stark shift grows sublinearly with increasing B, tends to saturation at large fields, and then decreases at even larger fields, when the reduction of d_{eh} is faster than $\propto 1/B$. The diamagnetic

shift dependence changes from quadratic to linear in B with increasing magnetic field. At large B, the exciton diamagnetic shift is equal to the one of a free electron modified by logarithmic corrections due to effective 1D Coulomb attraction to the hole [28].

Here we provide a brief comparison of the theoretical and experimental magneto-Stark slope $\beta' K_x$ at low magnetic fields to illustrate that the model is reasonable. A comparison to the full experimental field dependence of the diamagnetic and magneto-Stark shifts will be given in Sec. IV. The experimental value of the parameter $\beta'_{\rm exp} K_x \approx 350$ μeV/T measured in the pyramid SF [6] corresponds to $\beta'_{th} K_x$ for a reasonable set of values, i.e., $m_{h,\parallel} = 0.1\, m_0$, $V_0 = 7$ meV using the experimental value of $|K_x| \approx 1.6 \times 10^5$ cm^{-1}. The choice of parameters is not unique. For example, the same value of the magneto-Stark slope can be achieved at $m_{h,\parallel} = 0.14\, m_0$ and $V_0 = 10$ meV. This ambiguity is related to the fact that the exciton mass and the electron-hole distance enter only as a combination d_{eh}/M, thus, simultaneous increase of the exciton mass and electron-hole separation (by increasing the band offset V_0, [see Fig. 3(b)] results in the same value of β' in Eq. (16). We leave $m_{h,\parallel}$ as a free parameter of our model, since the calculation of $m_{h,\parallel}$ requires the knowledge of the full valence band spectrum for z-motion, and is out of scope of the present paper (see Supplementary Material of Ref. [6] for details).

The value of the electric field inside the SF that corresponds to $V_0 = 10$ meV and the width of SF 10 Å (see Appendix B for details) is $F \approx 0.1$ MV/cm, which is in line with the experiments on polytypic GaAs nanowires, where F lies in the range of 0.18 to 0.27 MV/cm [18]. On the other hand, this electric field is about five times smaller than in ZnSe SFs [23] and about 25 times smaller than in GaN SFs [16].

C. Double stacking fault

Besides the pyramid configuration, when SF planes are isolated, SFs can appear in a form of closely lying parallel planes, Fig. 1(b). In this trapezoid configuration, an exciton is bound to a double SF potential sketched in Fig. 2(b). We model this potential as a sum of two single SF potentials with the same band offset:

$$V_{\rm 2SF}(z_e, z_h) = V_{\rm SF}(z_e, z_h) + V_{\rm SF}(z_e - L, z_h - L), \qquad (17)$$

where L is a separation between SF planes, and $V_{\rm SF}$ is a single SF potential given by Eq. (3). The assumption that both SFs in a pair have the same direction of the built-in electric field follows from the experimentally observed approximately double increase of the exciton electric dipole moment as compared to the single SF case (see Sec. IV B for details) and the DFT calculations (see Appendix B).

We assume that the separation between the SFs is of the order of the hole confinement length in the z-direction a_h, which is around a few nanometers, but is much smaller than the electron-hole separation d_{eh}, which is of the order of tens of nanometers. In that case, an electron "sees" the double SF structure as a single SF with a twice-increased built-in electric field (band offset equal to $2V_0$), and hence, as it follows from Fig. 3, the d_{eh} parameter for a double SF also increases approximately twofold. On the other hand, the hole energy depends significantly on the SF separation. If $L \gg a_h$, the hole resides at the SF at $z_h = 0$ and does not "feel" another SF. With the decrease of L, when $L \sim a_h$, the hole confinement energy increases and its wave function is distributed over both SFs. In the limit $L = 0$, the hole energy is found from Eq. (4) with $u_0 \to 2u_0$ and $V_0 \to 2V_0$, respectively. The dependence of hole confinement energy ε_h on L is shown in Fig. 5.

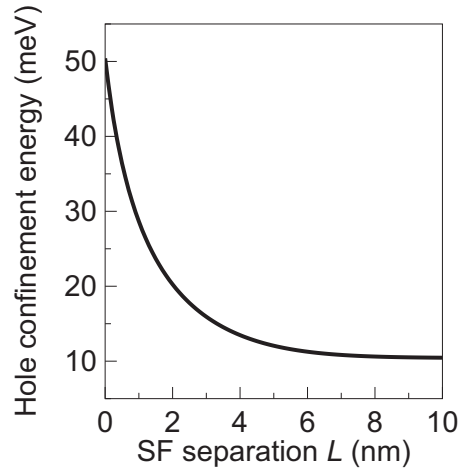

FIG. 5. Hole confinement energy as a function of SF separation. $V_0 = 10$ meV, $\varepsilon_0 = 15$ meV.

The scheme of exciton optical recombination is sketched in Fig. 2. The transition energies of an exciton bound to single and double SFs are

$$\begin{aligned} \hbar\omega_1 &= E_g - V_0 - \varepsilon_{h1} - \varepsilon_{B1}, \\ \hbar\omega_2 &= E_g - 2V_0 - \varepsilon_{h2} - \varepsilon_{B2}, \end{aligned} \qquad (18)$$

where $\varepsilon_{h1(2)}$ is the confinement energy of a hole bound to a single (double) SF potential, and $\varepsilon_{B1(2)}$ is the corresponding exciton binding energy. Neglecting the difference between SF and bulk exciton binding energies, the shifts of SF-bound exciton photoluminescence (PL) lines with respect to the bulk one are $\hbar\omega_X^{3D} - \hbar\omega_1 \approx V_0 + \varepsilon_{h1}$ and $\hbar\omega_X^{3D} - \hbar\omega_2 \approx 2V_0 + \varepsilon_{h2}$.

IV. COMPARISON TO EXPERIMENT

A. Magnetophotoluminescence

PL spectra taken at different magnetic fields are studied to verify the microscopic model. The molecular-beam-epitaxy (MBE)-grown GaAs sample [6] is mounted in a continuous helium flow cryostat at 1.5 K with a variable magnetic field from 0 to 7 T. PL from both pyramid and trapezoid 10-μm-scale SF structures is clearly resolved using an optical confocal setup with a resolution of $\sim$1 μm. The experimental geometry and typical PL spectra at $B = 0$ and $B = \pm 7$ T are shown in Fig. 6. The crystal [001] direction is perpendicular to the magnetic field $\boldsymbol{B} \parallel [\bar{1}10]$ and parallel to the optical axis. The collected SF PL corresponds to excitons with in-plane momentum

$$K_x = \frac{\omega n}{c} \sin\theta_{\rm SF}, \qquad (19)$$

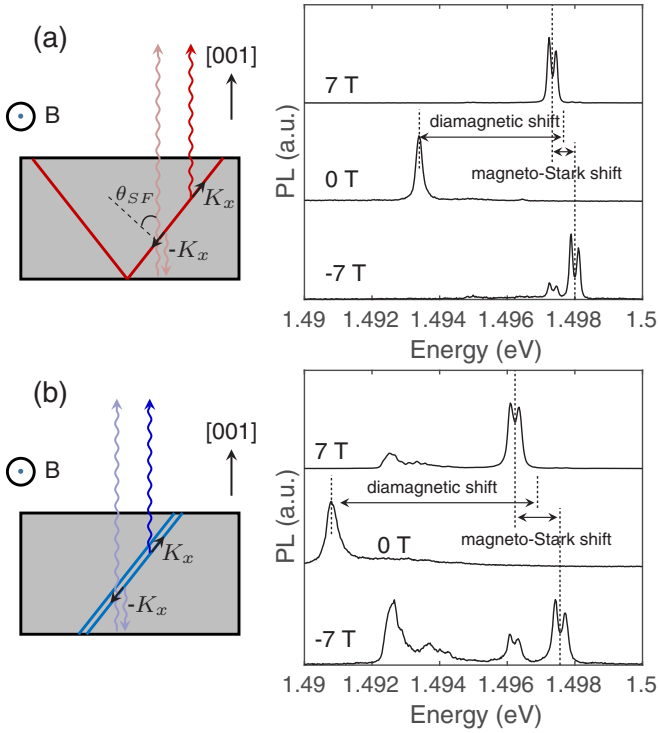

FIG. 6. Experimental geometry and PL spectrum of the (a) pyramid and (b) trapezoid structure. PL collected from $-K_x$ exciton is much weaker than PL from $+K_x$ exciton. The temperature is 1.5 K. The excitation laser is at 810 nm (1.53 eV).

where $\theta_{SF} = 54.7^\circ$ is the angle between the SF normal and the emitted photon momentum, ω is the photon frequency, n is the refractive index, and c is the speed of light. The collected PL from excitons with a wave vector $-K_x$ is much weaker than the PL from $+K_x$ excitons, because $-K_x$ excitons emit photons propagating toward the substrate and only backscattered light can be collected.

The magneto-PL spectra have similar properties for both the pyramid and trapezoid structures. At $B = 0$ T, a single PL peak is observed due to the recombination of excitons bound to the SF plane. At $B = \pm 7$ T, the main peak is split into a doublet due to the electron Zeeman splitting. At $B = -7$ T, in addition to the main doublet, a weaker doublet is observed at lower energy. This doublet has the same energy as the peak at $B = 7$ T, and thus, is attributed to excitons with $-K_x$ momentum. The origin of the peaks near $\hbar\omega = 1.4925$ eV observed in the trapezoid structure at $B = \pm 7$ T is unknown. The diamagnetic and magneto-Stark shifts are clearly observed in the magneto-PL spectra, as illustrated in Fig. 6. Figure 7 shows these experimental shifts as a function of magnetic field. The B-field dependence of diamagnetic and magneto-Stark shifts is in agreement with the microscopic model presented in Sec. III B, i.e., at low field the diamagnetic shift is $\propto B^2$ and the magneto-Stark shift is $\propto B$, whereas at high field diamagnetic shift tends to a linear B-dependence and the magneto-Stark shift exhibits a sublinear B dependence. The origin of the change at high field is the decrease of the electron-hole separation d_{eh} induced by the magnetic field.

By fixing $m_{h,\parallel} = 0.14\, m_0$ and using $V_0 = 10$ meV to fit the slope of the magneto-Stark shift at low magnetic fields,

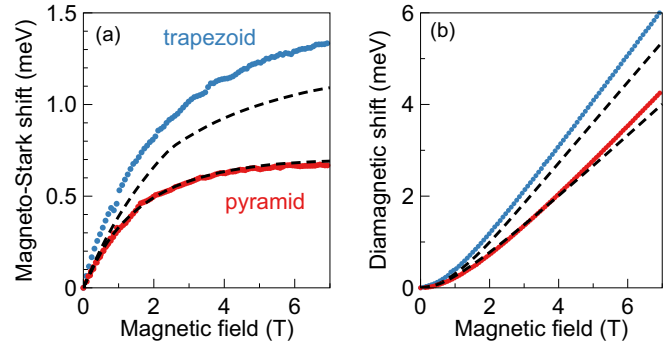

FIG. 7. Comparison of experiment (points) and theory (dashed lines) for pyramid and trapezoid SFs. The parameters used in calculations are $m_{h,\parallel} = 0.14\, m_0$, $V_0 = 10$ meV for pyramid SF, and $m_{h,\parallel} = 0.14\, m_0$, $V_0 = 20$ meV for trapezoid SF, respectively.

we obtain a qualitative agreement between the experimental and theoretical data for the pyramid structure at both low and high B-fields, as shown by the dashed lines in Fig. 7. As suggested by the double SF model presented in Sec. III C, an electron in the trapezoid SF experiences the twofold increase of the electric field as compared to the pyramid SF. By taking $m_{h,\parallel} = 0.14\, m_0$ and $V_0 = 20$ meV, we obtain a reasonable agreement between the experimental and theoretical data for the trapezoid structure, see Fig. 7. The larger value of the magneto-Stark shift in the experiment as compared to the theory might be caused by several reasons. One of the reasons is that the trapezoid structure consists of extrinsic and intrinsic SFs, see Fig. 1(c), which may have different values of V_0. Thus, the actual increase of effective electric field in the double SF as compared to the single one might be larger than two. Another reason might be a slight increase of d_{eh} with increased SF separation, which is not taken into account in the theory.

B. Variance of PL in trapezoid structures

The PL properties from different trapezoid structures exhibit a large variance relative to the pyramid structures. This is attributed to the variable separation between the two parallel SF planes. Figure 8(a) shows the distribution of 0 T PL energies for 133 different trapezoid structures and five different pyramid structures (corresponding to 20 single SF planes). For the pyramid structures, the SF excitons only emit at PL energy $E_{SF} = 1.4928$ and 1.4959 eV. For the trapezoid structures, E_{SF} varies from 1.487 to 1.491 eV. Between 1.4875 and 1.4891 eV, four discrete energies are observed: 1.4875, 1.4882, 1.4887, and 1.4891 eV. At higher energies, the distribution is continuous.

To further understand this effect, the trapezoid PL intensity and electron-hole separation are investigated, as shown in Figs. 8(b) and 8(c). The electron-hole separation is derived from the magneto-Stark shift, see Eq. (16). Throughout this discussion, we assume $M = 0.17 m_0$, which corresponds to $m_{h,\parallel} = 0.1\, m_0$ and the electron effective mass $m_e = 0.07\, m_0$. The electron-hole separation for the trapezoid is approximately double that of the pyramid and it slightly increases with E_{SF}. The PL intensity for trapezoids emitting at one

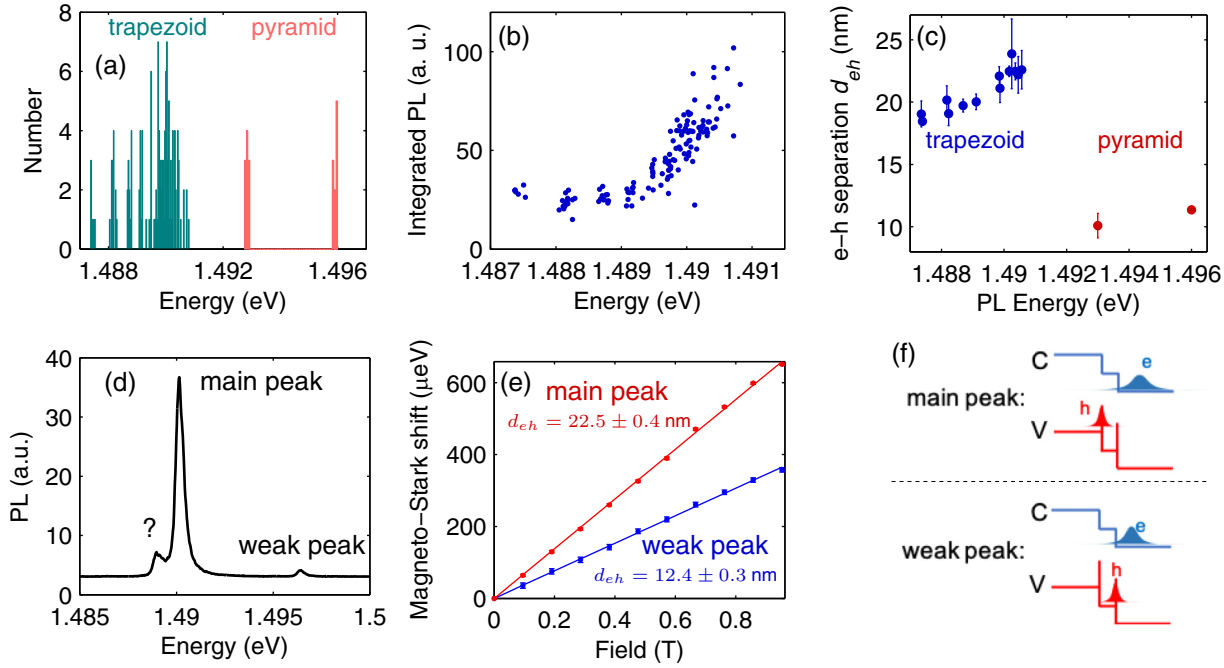

FIG. 8. (a) Distribution of the PL energy for excitons bound to the trapezoid and pyramid structures. 1.5 K. 810 nm excitation. (b) PL intensity as a function of E_{SF}. (c) Electron-hole separation as a function of the E_{SF} for trapezoid and pyramid structures. The electron-hole separation is measured by the magneto-Stark effect and the calculation uses in-plane exciton mass $0.17m_0$. (d) PL spectrum of a trapezoid with high PL energy. The peak marked by the question mark is unknown and does not exhibit magneto-Stark effect. (e) Magneto-Stark shift as a function of magnetic field for the main peak and second peak. The calculated e-h separation d_{eh} is listed in the figure. (f) Illustration of the exciton wave function for excitons of the two different peaks. C: conduction band. V: valence band. e: electron. h: hole.

of the four discrete energies does not change with E_{SF}. In contrast, for trapezoids with $E_{SF} > 1.4891$ eV, the intensity increases with increasing E_{SF}. We further note that for these high-energy trapezoids, the PL spectra contain two distinct SF exciton peaks, as shown in Fig. 8(d). The main peak corresponds to an exciton with electron-hole separation of 22.5 nm and the weak peak corresponds to an electron-hole separation of 12.4 nm. Possibly, this can be attributed to two different electron locations, as shown in Fig. 8(f). The quantitative analysis of the interplay between the main and the weak peaks is beyond the scope of this work. For trapezoids with PL energy at one of the four discrete values between 1.4875 to 1.4891 eV, the second peak is not observed. We attribute this to a higher tunneling rate from the metastable (weak peak) configuration to the stable configuration (main peak) or a delocalization of the hole wave function over both faults (Sec. III C when the two SFs are close.)

It follows from the microscopic model shown in Sec. III C that the doubling of d_{eh} of the double SF compared to the single SF is due to the existence of the double step potentials and the small separation between two SFs. Such a shape of potential leads to approximately twofold increase of the electric field experienced by an electron. On the other hand, the experimentally observed spread of emission energy is mainly caused by the variation of the hole confinement energy with the distance between two SFs. Comparison between the theoretical dependence, shown in Fig. 5, and the experimental distribution of the exciton emission energy suggests that the SF separation is around $4 - 6$ nanometers. This conclusion is also confirmed by the STEM data on trapezoid SFs shown in Fig. 1(c), where the distance of ≈5.5 nm between the SFs is measured.

As shown in Fig. 5, with the increase of the SF separation, the hole confinement energy decreases and, thus, the exciton emission energy, see Eqs. (18), increases. The spread of the hole wave function also increases with larger SF separation, leading to larger electron-hole wave function overlap, and thus, the increase of the PL intensity. These conclusions qualitatively agree with the continuously distributed data ($E_{SF} > 1.4891$ nm) shown in Figs. 8(a)–8(c). A slight increase of d_{eh} with the PL energy, observed in Fig. 8(c), may be attributed to increased SF separation. The origin is still not clear for the four discretely distributed PL energies, i.e., $E_{SF} =$ 1.4875, 1.4882, 1.4887, and 1.4891 eV. A plausible theory is that only certain SF separations are energetically allowed for forming stable double SF structures if the SF separation is small. This theory could be further confirmed by a correlated optical-structural imaging study of several trapezoid structures.

V. CONCLUSION

In conclusion, we have developed a microscopic model of the SF potential and exciton wave function in GaAs. Specifically, the SF potential provides a delta-function-like confinement for the hole and a steplike potential for the electron. Variational method calculations for the exciton diamagnetic and magneto-Stark shifts show good agreement

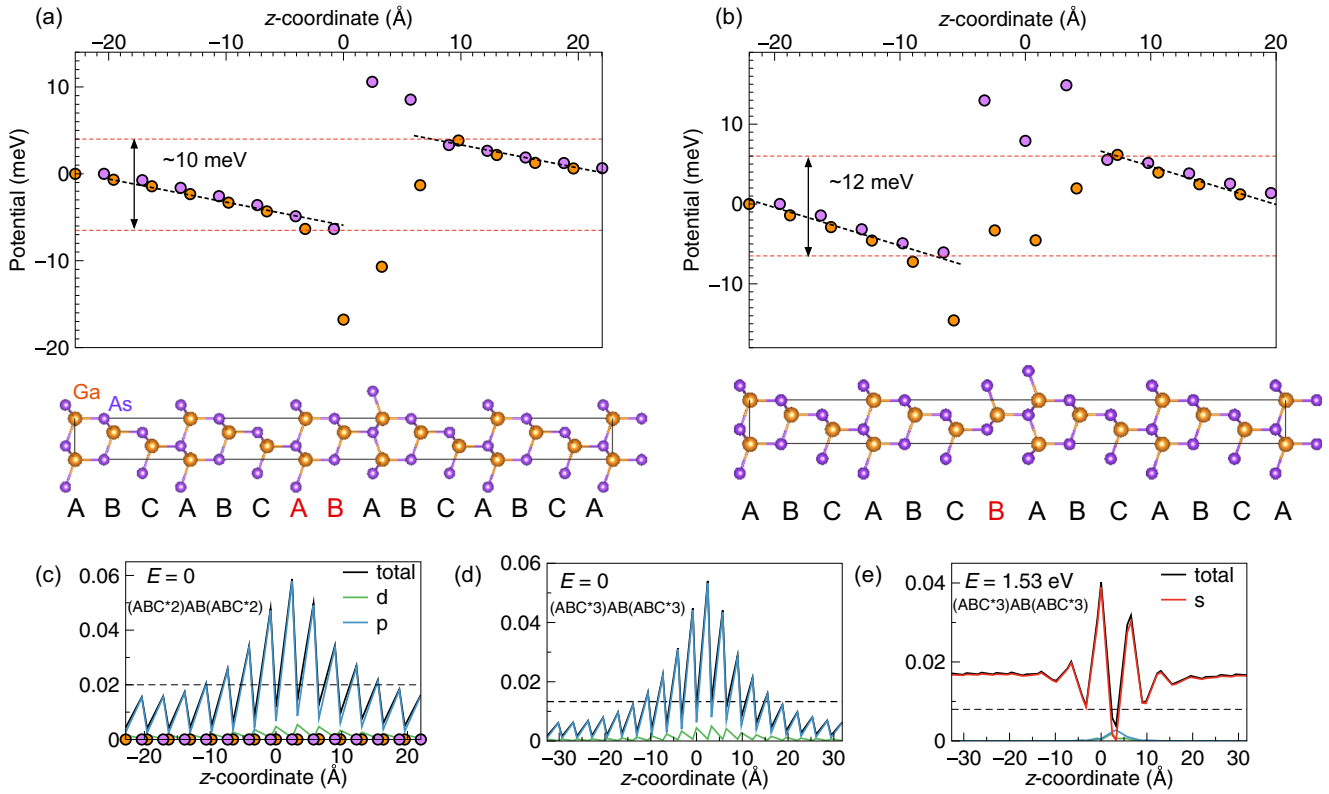

FIG. 9. Summary of the DFT calculations. (a), (b) Electrostatic potential of the *intrinsic* (a) and *extrinsic* (b) SFs extracted from the DFT calculations. The insets in the bottom show the elementary cells used in the calculation. (c)–(e) Electron density of s, p, and d atomic orbitals in the states with different energies in the *intrinsic* stacking fault. $E = 0$ is the position of the Fermi level, and $E = 1.53$ eV is the lowest unoccupied state. The black curve is the sum of s, p, and d contributions, the dashed horizontal line depicts the electron density in the interstitial (interatomic) region. Panels (d), (e) correspond to a stacking fault structure with six additional monolayers as compared to other panels.

between theory and experiment for the single SF potential. This comparison together with DFT calculations of electronic spectrum allowed us to estimate the band offset at the SF plane as ∼10 meV, which corresponds to the built-in electric field $F \sim 0.1$ MV/cm. The model also qualitatively describes the twofold increase in the exciton dipole moment observed in the double SF structure, suggesting an average inter-fault distance of $4 - 6$ nm. This value is also confirmed by the STEM measurements of the trapezoid SFs. The properties of SF excitons not only have implications for improving GaAs technologies such as solar cells and LEDs [3–5,29], but also provide insight into understanding potential exciton-exciton interactions and whether new excitonic phases are accessible in this system or similar systems [30,31].

ACKNOWLEDGMENTS

We acknowledge C. Johnson for his assistance in the experimental measurements. M.V.D. is grateful to Dr. M.O. Nestoklon for fruitful discussions and help with DFT calculations. TEM experiments and modeling were supported by Pacific Northwest National Laboratory (PNNL) Directed Research and Development program. PNNL is operated by Battelle for the Department of Energy under Contract No. DE-AC05-76RLO1830. STEM imaging was performed in the Radiological Microscopy Suite (RMS), located in the Radiochemical Processing Laboratory (RPL) at PNNL. M.V.D. acknowledges financial support from the Basis Foundation for the Advancement of Theoretical Physics and Mathematics and the Russian Federation President Grant No. MK-2943.2019.2. M.M.G. and M.V.D. have also been partially supported by the RFBR Grant No. 17-02-00383 and by the Program No. 13 of Presidium of RAS. K.M.C.F., X.L., and M.L.K.V. acknowledge support by the UW Molecular Engineering and Materials Center with funding from the NSF MRSEC program (No. DMR-1719797). A.D.W. and A.L. acknowledge gratefully support of DFG-TRR160, BMBF-Q.Link.X 16KIS0867, and the DFH/UFA CDFA-05-06.

APPENDIX A: STRUCTURAL IMAGING

Cross-sectional STEM samples were prepared using a FEI Helios NanoLab DualBeam Focused Ion Beam microscope and a standard lift-out procedure along the GaAs [110] zone axis, with initial cuts made at 30 kV and final polishing at 2 kV. High-angle annular dark field images were collected on a probe-corrected JEOL GrandARM-300F microscope operating at 300 kV, with a convergence semiangle of 29.7 mrad, and a collection angle of 72–495 mrad. To minimize scan artifacts and improve signal to noise, drift-corrected images were prepared using the SmartAlign plugin [32] for this, a series of ten frames at 1024 × 1024 pixels with a 2 µs px^{-1}

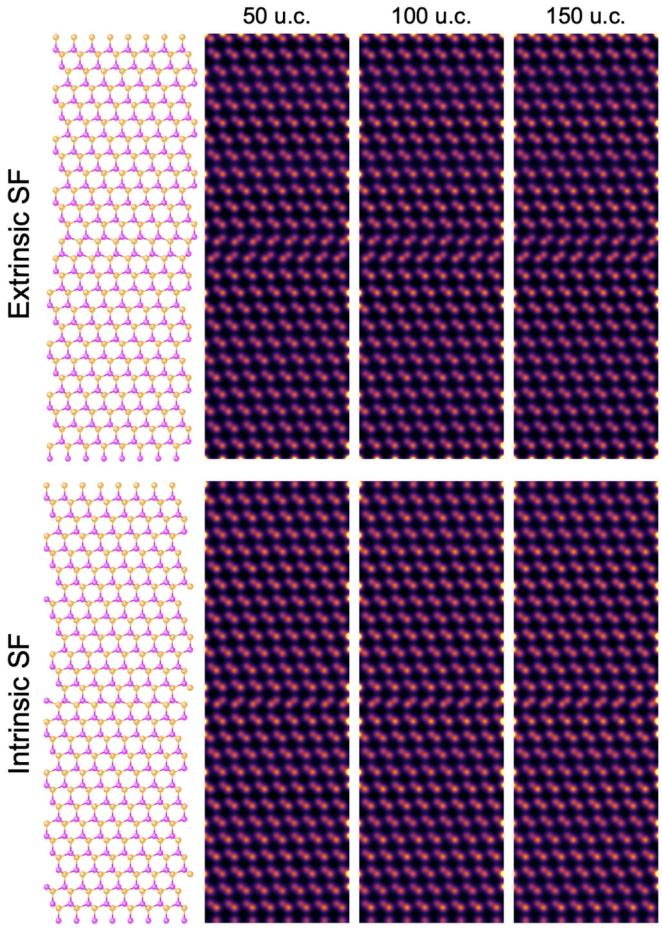

FIG. 10. Series of multislice image simulations performed for the extrinsic (top) and intrinsic (bottom) stacking fault structures for 50-, 100-, and 150-u.c.-thick crystals using the PRISM code.

dwell time and 90° rotation between frames was used. The frames were upsampled two times prior to nonrigid alignment, followed by template matching parallel to the fault direction. Full multislice image simulations were conducted with the PRISM code [33] for several candidate structures from *ab initio* calculations. Simulations were performed using a 1×4 tiling for crystal thicknesses of 50, 100, and 150 u.c., corresponding to 20, 40, and 60 nm, respectively. Imaging parameters were matched to the experiment and a 0.05 Å px^{-1} sampling, 2 Å slice thickness, and ten frozen phonon passes were used for the final simulations. From these simulations, the 60-nm simulation was compared to the experiment.

We have performed a series of multislice image simulations based upon our *ab initio* calculations for both the extrinsic and intrinsic SF structures. Simulations were conducted across a range of reasonable sample thicknesses, using the same experimental imaging conditions, as shown in Fig. 10. We find a good agreement between the real and simulated structures, supporting the validity of our calculations. We observe only subtle changes in image contrast with increasing thickness and find that the 150-u.c. model is most consistent with our prior knowledge of the sample and the measured data.

APPENDIX B: DFT CALCULATIONS OF THE STACKING FAULT ELECTRONIC STRUCTURE

To estimate the value of the band offset V_0 and analyze single-electron states in the presence of the SF, we performed the DFT calculations using the WIEN2K package with mBJ exchange-correlation potential [34,35]. We performed calculations for two types of stacking faults, an intrinsic and an extrinsic one, that have a different order of layers in the vicinity of the stacking fault; see the insets of Figs. 9(a) and 9(b). To estimate the electrostatic potential in the stacking fault structure, we applied the procedure described in Refs. [23,36,37], which involves tracking the position of the core $1s$ level at Ga and As atoms in the structure. The presented calculations were performed for relaxed structures, however, we found that the value of V_0 is only slightly different in relaxed and nonrelaxed structures. The calculations predict that the energy gap of the bulk zinc-blende phase is about 200 meV larger than that of the bulk wurtzite phase. This result differs from the results of most DFT calculations known from literature, which predict a larger energy gap of the bulk wurtzite phase, e.g., ≈32 meV difference obtained in Ref. [20]. This discrepancy is probably due to the simplified version of the DFT procedure we use. To obtain more accurate values of fundamental gaps, one should use more sophisticated methods (such as GW corrections or LDA-1/2). However, for the ground-state calculations which we perform here, our simplified approach seems to be reasonable.

The extracted electrostatic potential is shown in Figs. 9(a) and 9(b). In agreement with previous results on the ZnSe stacking faults [23], we observe an overall jump of electrostatic potential when crossing the stacking fault region. The linear behavior of the potential, i.e., nonzero electric field, outside the stacking fault region is an artifact of periodic boundary conditions used in numeric calculations. We checked that this field decreases with an increase of the elementary cell length. The oscillations of the potential and, correspondingly, of the electric field in the vicinity of the stacking fault, are not eliminated by the increase of the calculation accuracy and the cell length. These oscillations reflect the atomic-scale oscillations of the charge density in the stacking fault region. The electrostatic potential change across the SF, which corresponds to the V_0 parameter in Eq. (3), is $V_0 \approx 10$ meV and has the same sign for both intrinsic and extrinsic stacking faults. The corresponding electric field inside the SFs is ≈0.1 MV/cm, which is about five times smaller than in ZnSe SFs [23] and about 25 times smaller than in GaN SFs [16].

Figures 9(c)–9(e) show the behavior of the electron density across the stacking fault. It is seen that the lowest state in the conduction band is delocalized, whereas the highest state in the valence band is localized with the localization length $a_h \approx 40$ Å (full width of density at $1/e^2$). We checked that a_h does not depend on the supercell size, see Figs. 9(d) and 9(e). Hence, the stacking fault tightly binds a heavy hole and does not localize an electron, in agreement with the suggested model potential Eq. (3). Using $m_{h,\perp} \approx 0.95 m_0$ [15], the hole confinement energy $\varepsilon_h = 2\hbar^2/(m_{h,\perp} a_h^2) \approx 10$ meV. The energy shift between the bulk exciton and SF exciton is $\varepsilon_h + V_0 \approx 20$ meV, which agrees well with the experimental value ≈19 to 22 meV.

[1] R. Jamaati and M. R. Toroghinejad, Effect of stacking fault energy on mechanical properties of nanostructured FCC materials processed by the ARB process, Mater. Sci. Eng. A **606**, 443 (2014).

[2] J. Yang, G. W. Neudeck, and J. P. Denton, Electrical effects of a single stacking fault on fully depleted thin-film silicon-on-insulator P-channel metal-oxide-semiconductor field-effect transistors, J. Appl. Phys. **91**, 420 (2002).

[3] P. Caroff, J. Bolinsson, and J. Johansson, Crystal phases in III–V nanowires: From random toward engineered polytypism, IEEE J. Sel. Top. Quantum Electron. **17**, 829 (2011).

[4] S. Guha, J. M. DePuydt, M. A. Haase, J. Qiu, and H. Cheng, Degradation of II-VI based blue-green light emitters, Appl. Phys. Lett. **63**, 3107 (1993).

[5] A. Colli, E. Pelucchi, and A. Franciosi, Controlling the native stacking fault density in II-VI/III-V heterostructures, Appl. Phys. Lett. **83**, 81 (2003).

[6] T. Karin, X. Linpeng, M. M. Glazov, M. V. Durnev, E. L. Ivchenko, S. Harvey, A. K. Rai, A. Ludwig, A. D. Wieck, and Kai Mei C. Fu, Giant permanent dipole moment of two-dimensional excitons bound to a single stacking fault, Phys. Rev. B **94**, 041201(R) (2016).

[7] L. V. Butov, C. W. Lai, A. L. Ivanov, A. C. Gossard, and D. S. Chemla, Towards Bose-Einstein condensation of excitons in potential traps, Nature (London) **417**, 47 (2002).

[8] L. V. Butov, A. C. Gossard, and D. S. Chemla, Macroscopically ordered state in an exciton system, Nature (London) **418**, 751 (2002).

[9] D. G. Thomas and J. J. Hopfield, Direct Observation of Exciton Motion in CdS, Phys. Rev. Lett. **5**, 505 (1960).

[10] E. F. Gross, B. P. Zakharchenya, and O. V. Konstantinov, Effect of magnetic field inversion in spectra of exciton absorption in CdSe crystal, Sov. Phys. Solid State **3**, 221 (1961).

[11] M. Lafrentz, D. Brunne, B. Kaminski, V. V. Pavlov, A. V. Rodina, R. V. Pisarev, D. R. Yakovlev, A. Bakin, and M. Bayer, Magneto-Stark Effect of Excitons as the Origin of Second Harmonic Generation in ZnO, Phys. Rev. Lett. **110**, 116402 (2013).

[12] J. ichi Kasai and M. Kawata, Microphotoluminescence of oval defects in a GaAs layer grown by molecular beam epitaxy, Appl. Phys. Lett. **73**, 2012 (1998).

[13] E. L. Ivchenko and G. E. Pikus, *Superlattices and other Heterostructures* (Springer, Berlin, Germany, 1997).

[14] E. L. Ivchenko, *Optical Spectroscopy of Semiconductor Nanostructures* (Alpha Science, Harrow, UK, 2005).

[15] Z. Ikonic´, V. Milanovic´, and D. Tjapkin, Valence subband structure of [100]-, [110]-, and [111]-grown GaAs-(Al, Ga)As quantum wells and the accuracy of the axial approximation, Phys. Rev. B **46**, 4285 (1992).

[16] J. Lähnemann, O. Brandt, U. Jahn, C. Pfüller, C. Roder, P. Dogan, F. Grosse, A. Belabbes, F. Bechstedt, A. Trampert, and L. Geelhaar, Direct experimental determination of the spontaneous polarization of GaN, Phys. Rev. B **86**, 081302(R) (2012).

[17] A. Belabbes, J. Furthmüller, and F. Bechstedt, Relation between spontaneous polarization and crystal field from first principles, Phys. Rev. B **87**, 035305 (2013).

[18] B. Bauer, J. Hubmann, M. Lohr, E. Reiger, D. Bougeard, and J. Zweck, Direct detection of spontaneous polarization in wurtzite GaAs nanowires, Appl. Phys. Lett. **104**, 211902 (2014).

[19] D. Spirkoska, J. Arbiol, A. Gustafsson, S. Conesa-Boj, F. Glas, I. Zardo, M. Heigoldt, M. H. Gass, A. L. Bleloch, S. Estrade, M. Kaniber, J. Rossler, F. Peiro, J. R. Morante, G. Abstreiter, L. Samuelson, and A. Fontcuberta I Morral, Structural and optical properties of high quality zinc-blende/wurtzite GaAs nanowire heterostructures, Phys. Rev. B **80**, 245325 (2009).

[20] A. Belabbes, C. Panse, J. Furthmüller, and F. Bechstedt, Electronic bands of III-V semiconductor polytypes and their alignment, Phys. Rev. B **86**, 075208 (2012).

[21] M. Heiss, S. Conesa-Boj, J. Ren, H.-H. Tseng, A. Gali, A. Rudolph, E. Uccelli, F. Peiró, J. R. Morante, D. Schuh, E. Reiger, E. Kaxiras, J. Arbiol, and A. Fontcuberta I Morral, Direct correlation of crystal structure and optical properties in wurtzite/zinc-blende GaAs nanowire heterostructures, Phys. Rev. B **83**, 045303 (2011).

[22] O. Marquardt, M. Ramsteiner, P. Corfdir, L. Geelhaar, and O. Brandt, Modeling the electronic properties of GaAs polytype nanostructures: Impact of strain on the conduction band character, Phys. Rev. B **95**, 245309 (2017).

[23] D. S. Smirnov, K. G. Belyaev, D. A. Kirilenko, M. O. Nestoklon, M. V. Rakhlin, A. A. Toropov, I. V. Sedova, S. V. Sorokin, S. V. Ivanov, B. Gil, and T. V. Shubina, Exciton bound to 1d intersection of stacking fault plane with a ZnSe quantum well, Phys. Status Solidi RRL **12**, 1700410 (2018).

[24] L. P Gor'kov and I. E. Dzyaloshinskiy, Contribution to the theory of the Mott exciton in a strong magnetic field, Sov. Phys. JETP **26**, 449 (1968).

[25] M. de Dios-Leyva, C. A. Duque, and L. E. Oliveira, Calculation of direct and indirect excitons in GaAs/GaAlAs coupled double quantum wells: The effects of in-plane magnetic fields and growth-direction electric fields, Phys. Rev. B **76**, 075303 (2007).

[26] A. A. Gorbatsevich and I. V. Tokatly, Formation of k-space indirect magnetoexcitons in double-quantum-well direct-gap heterostructures, Semicond. Sci. Technol. **13**, 288 (1998).

[27] K. Chang and F. M. Peeters, Bright-to-dark exciton transition in symmetric coupled quantum wells induced by an in-plane magnetic field, Phys. Rev. B **63**, 153307 (2001).

[28] L. D. Landau and E. M. Lifshitz, *Quantum Mechanics: Non-Relativistic Theory* (Pergamon Press, Oxford, UK, 1977), Vol. 3.

[29] T. Karin, X. Linpeng, A. K. Rai, A. Ludwig, A. D. Wieck, and K. C. Fu, Optical visualization of radiative recombination at partial dislocations in GaAs, in 2016 IEEE 43rd Photovoltaic Specialists Conference (PVSC) (Institute of Electrical and Electronics Engineers, Red Hook, NY, USA, 2016), pp. 1989–1992.

[30] J. M. Kosterlitz and D. J. Thouless, Ordering, metastability and phase transitions in two-dimensional systems, J. Phys. C : Solid State Phys. **6**, 1181 (1973).

[31] A. A. High, A. K. Thomas, G. Grosso, M. Remeika, A. T. Hammack, A. D. Meyertholen, M. M. Fogler, L. V. Butov, M. Hanson, and A. C. Gossard, Trapping Indirect Excitons in a GaAs Quantum-Well Structure with a Diamond-Shaped Electrostatic Trap, Phys. Rev. Lett. **103**, 087403 (2009).

[32] L. Jones, H. Yang, T. J. Pennycook, M. S. J. Marshall, S. V. Aert, N. D. Browning, M. R. Castell, and P. D. Nellist, Smart align—a new tool for robust non-rigid registration of scanning microscope data, Adv. Struct. Chem. Imaging **1**, 8 (2015).

[33] A. Pryor, C. Ophus, and J. Miao, A streaming multi-GPU implementation of image simulation algorithms for scanning transmission electron microscopy, Adv. Struct. Chem. Imaging **3**, 15 (2017).

[34] P. Blaha, K. Schwarz, G. K. H. Madsen, D. Kvasnicka, and J. Luitz, *WIEN2K, An Augmented Plane Wave + Local Orbitals Program for Calculating Crystal Properties* (Karlheinz Schwarz, Techn. Universität Wien, Austria, 2001).

[35] F. Tran and P. Blaha, Accurate Band Gaps of Semiconductors and Insulators with a Semilocal Exchange-Correlation Potential, Phys. Rev. Lett. **102**, 226401 (2009).

[36] S.-H. Wei and A. Zunger, Role of d Orbitals in Valence-Band Offsets of Common-Anion Semiconductors, Phys. Rev. Lett. **59**, 144 (1987).

[37] Y.-H. Li, A. Walsh, S. Chen, W.-J. Yin, J.-H. Yang, J. Li, J. L. F. Da Silva, X. G. Gong, and S.-H. Wei, Revised ab initio natural band offsets of all group IV, II-VI, and III-V semiconductors, Appl. Phys. Lett. **94**, 212109 (2009).